This article has been accepted for publication in IEEE Open Journal of Signal Processing. This is the author's version which has not been fully edited and content may change prior to final publication. Citation information: DOI 10.1109/OJSP.2024.3425284

Received XX Month, XXXX; revised XX Month, XXXX; accepted XX Month, XXXX; Date of publication XX Month, XXXX; date of current version XX Month, XXXX.

Digital Object Identifier 10.1109/XXXX.2022.1234567

Difference frequency gridless sparse array processing

Yongsung Park[1], Member, IEEE and Peter Gerstoft[1], Fellow, IEEE

[1]NoiseLab at the Scripps Institution of Oceanography, University of California San Diego, La Jolla, CA 92093 USA

Corresponding author: Yongsung Park (email: yongsungpark@ ucsd.edu).

This work was supported by the Office of Naval Research, Grant No. N00014-21-1-2267.

ABSTRACT This paper introduces a DOA estimation method for sources beyond the aliasing frequency. The method utilizes multiple frequencies of sources to exploit the frequency difference between them, enabling processing at a frequency below the aliasing frequency. Gridless sparse processing with atomic norm minimization is derived for DOA with difference frequency (DF). This approach achieves higher DOA resolution than previous DF-DOA estimators by enforcing sparsity in the beamforming spectrum and estimating DOAs in the continuous angular domain. We consider one or more measurements in both time (snapshot) and frequency (DF). We also analyze approaches for considering multiple DFs: multi-DF and multi-DF spectral-averaging. Numerical simulations demonstrate the effective performance of the method compared to existing DF techniques.

INDEX TERMS Difference frequency, DOA estimation, spatial aliasing, atomic norm minimization.

I. INTRODUCTION

SPATIAL aliasing for DOA estimation requires the frequency to be less than $c/2d$ (velocity c and element spacing d), processing above gives ambiguous DOA estimates. Signals of interest can be out of band at higher frequencies, e.g., for passive array systems. We introduce a gridless sparse method for DOA with difference frequency (DF), which accurately estimates the DOAs of sources beyond the aliasing frequency.

The method utilizes a pair (or more) of multiple frequencies on the array. Multi-frequency processing leverages more information than one frequency, giving more accurate estimation [1]–[5]. An intuitive approach is to treat each frequency individually using single-frequency techniques and then average the DOAs across all frequencies to obtain the final DOAs. Methods that jointly handle multiple frequencies can outperform single-frequency methods.

The spectral properties of multi-frequency signals were used for DOA using co-prime arrays with improved performance. Multiple frequencies were used to fill in the elements of the virtual co-array, resulting in improved DOA performance [6]–[10]. Co-prime arrays use spacing differences between elements to obtain virtual co-array elements. Similarly, DF employs frequency differences to acquire virtual low frequencies. In co-arrays for one frequency, each virtual sensor response is obtained by multiplying the sensor data at one sensor with the complex conjugate at another. Co-array approach with high-order cumulant-based methods outperforms traditional second-order statistics methods as it suppresses noise and achieves virtual array expansion [11]–[17]. Similarly, in the DF framework, the data at one frequency at one sensor is multiplied with the complex conjugate at another frequency. This could lead to higher-resolution sensing, contributing to integrated sensing and communications [18].

Multi-frequency DF enables processing signals above the aliasing frequency f_{alias}. The technique utilizes sources with a pair of high frequencies $\{f, f+\Delta f\} > f_{\text{alias}}$, with the frequency difference Δf below the aliasing frequency $\Delta f < f_{\text{alias}}$. The received far-field on the array is assumed to be a superposition of plane waves. The frequency difference is then achieved by taking the product of the complex conjugate of the data at frequency f and the data at frequency $f+\Delta f$. This gives virtual data at the lowered frequency Δf, avoiding spatial aliasing [19]–[22].

The DF technique was used for array processing and validated experimentally [20]–[27]. For DOA, conventional beamforming (CBF) was employed [20]. The DF-CBF at frequency Δf lowered by DF showed comparable results to the CBF at frequency Δf without DF [23]. For source

This work is licensed under a Creative Commons Attribution 4.0 License. For more information, see https://creativecommons.org/licenses/by/4.0/

This work is licensed under a Creative Commons Attribution-NonCommercial-NoDerivatives 4.0 License. For more information, see https://creativecommons.org/licenses/by-nc-nd/4.0/

This article has been accepted for publication in IEEE Open Journal of Signal Processing. This is the author's version which has not been fully edited and content may change prior to final publication. Citation information: DOI 10.1109/OJSP.2024.3425284

localization, DF for matched field processing was demonstrated [28]–[30]. High-resolution DF-MUSIC (multiple signal classification) [21] and DF gridded sparse processing [22] were performed, but no gridless DF has been derived.

Gridless sparse beamforming [31]–[33] offers high-resolution DOAs. Sparse DOA methods can be extended to multi-frequency and have demonstrated improved performance over the single-frequency model [9], [34]–[39]. Gridded sparse methods [31], [40] for DOA suffer from basis grid mismatch when the true DOAs are not on the search grid, as discrete dictionaries do not represent the data [41]–[43]. Mitigating grid mismatch bias can be achieved by adaptive grid refinement [34], off-grid methods [44], and gridless methods [40], [41], [45], [46]. The gridless method leverages the mathematical theory of super-resolution and estimates DOAs in the continuous angle domain.

We present gridless atomic norm minimization (ANM) for DF-DOA for sources above the spatial aliasing frequency. While the DF approach provides aliasing-free DOA estimation, it generates unwanted (artifact) DOA estimates. An ideal DF DOA estimator should estimate both true and artifact DOAs, and further analysis should refine these DOAs to the true DOAs. In addition to numerical verification [Sec. VI], the key contributions are as follows:

1) We introduce DF-DOA and analyze the DOA characteristics caused by DF, providing insights for integrating the DF concept into state-of-the-art DOA estimators [Sec. III].

2) We formulate high-resolution DF-DOA estimation with ANM [40], [41], [45], [46]. This handles noise-corrupted data and provides mean-squared-error estimates for denoising beamforming spectra with the atomic norm [Sec. IV.B].

3) Multiple measurements in time and frequency are used. With multiple equally spaced frequency differences, multiple DFs with the same frequency difference and thus steering vectors. Like conventional multi-snapshot processing, where multiple snapshot data vectors are aligned in a matrix and processed, the multi-DF aligns and processes multiple DF data. This approach is expanded to the multi-snapshot-DF, where all multi-snapshot and multi-DF data are grouped and processed [Sec. V].

4) Multi-DF spectral-averaging (SA) is proposed for arbitrarily spaced multiple DFs by solving the multi-snapshot ANM for each frequency pair (DF) and obtaining null spectra to identify the DOA support of the sparse signals for each DF. Subsequently, the null spectra are averaged across DFs to extract DOA estimates. This method generalizes to non-uniformly spaced DFs and is simple and effective at high signal-to-noise ratios (SNRs). In contrast, at low SNR, the multi-snapshot-DF integrates DF data more effectively than the multi-snapshot-DF-SA [Sec. VI.E].

Notation: For a matrix $\mathbf{A}$, $\mathbf{A}^{\mathsf{T}}$ is the transpose, $\mathbf{A}^*$ the complex conjugate, and $\mathbf{A}^{\mathsf{H}}$ the conjugate transpose. The Hadamard products of matrices $\mathbf{A}$ and $\mathbf{B}$ is denoted $\mathbf{A}\circ\mathbf{B}$.

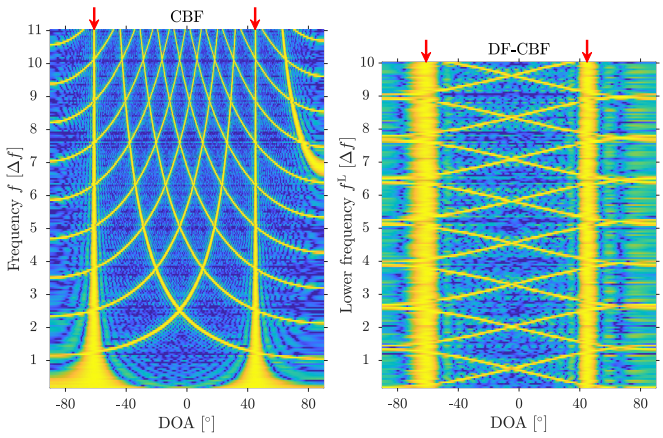

FIGURE 1. CBF and DF-CBF for $K=2$ equal-strength DOAs at $[-61,45]^\circ$ The ULA has $M=20$ sensors with a spacing d. The frequencies are measured using the spatial aliasing frequency $\Delta f=(c/d)/2$. CBF uses frequencies $f\in[0.2\Delta f,11\Delta f]$. DF-CBF uses a constant $\Delta f(=f^{\mathrm{U}}-f^{\mathrm{L}})$ with $f^{\mathrm{L}}\in[0.2\Delta f,10\Delta f]$ and $f^{\mathrm{U}}\in[1.2\Delta f,11\Delta f]$. Across frequencies, DF-CBF has constant $K^2=4$ DOAs, with K true and K^2-K artifact.

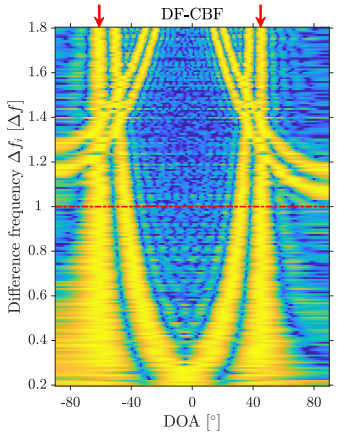

FIGURE 2. DF-CBF for Δf_i and potential DOAs. As in Fig. 1, but with different $\Delta f_i\in[0.2\Delta f,1.8\Delta f]$ using $f^{\mathrm{L}}=10\Delta f$ and $f^{\mathrm{U}}\in[10.2\Delta f,11.8\Delta f]$. DF-CBF has aliasing, when Δf_i exceeds the aliasing frequency ($=\Delta f$) (dash-dotted).

II. Array data model

Consider K DOAs with L snapshots at frequency f. We assume the sources with DOAs $\theta_k\in[-90^\circ,90^\circ)$ are in the far-field of a uniform linear array (ULA) with M sensors. Let $\mathbf{X}_f\in\mathbb{C}^{K\times L}$ be the complex source amplitudes, whose (k,l)-element is $x_{kt_l,f}\in\mathbb{C}$, $k=1,\dots,K$, $l=1,\dots L$, and the array data $\mathbf{Y}_f=[\mathbf{y}_{t_1,f}\dots\mathbf{y}_{t_L,f}]\in\mathbb{C}^{M\times L}$, where $\mathbf{y}_{t_l,f}=[y_{1t_l,f}\dots y_{Mt_l,f}]^{\mathsf{T}}\in\mathbb{C}^M$, is modeled as

$$\mathbf{Y}_f=\sum_{k=1}^{K}\mathbf{a}_f(\theta_k)\mathbf{x}_{kL,f}^{\mathsf{T}}+\mathbf{E}_f, \tag{1}$$

where $\mathbf{x}_{kL,f}=[x_{kt_1,f}\dots x_{kt_L,f}]^{\mathsf{T}}\in\mathbb{C}^L$, $\mathbf{E}_f=[\mathbf{e}_{t_1,f}\dots\mathbf{e}_{t_L,f}]\in\mathbb{C}^{M\times L}$, where $\mathbf{e}_{t_l,f}=[e_{1t_l,f}\dots e_{Mt_l,f}]^{\mathsf{T}}\in\mathbb{C}^M$, is the additive noise, and the steering vector,

$$\mathbf{a}_f(\theta)=\left[e^{-j2\pi f d_1\sin\theta/c}\dots e^{-j2\pi f d_M\sin\theta/c}\right]^{\mathsf{T}}\in\mathbb{C}^M, \tag{2}$$

This work is licensed under a Creative Commons Attribution-NonCommercial-NoDerivatives 4.0 License. For more information, see https://creativecommons.org/licenses/by-nc-nd/4.0/

This article has been accepted for publication in IEEE Open Journal of Signal Processing. This is the author's version which has not been fully edited and content may change prior to final publication. Citation information: DOI 10.1109/OJSP.2024.3425284.

where c is the velocity of propagation and $d_m=(m-1)d$, $m=1,\dots,M$, is the distance between sensors 1 and m with the ULA element spacing d. The additive noise $\mathbf{E}_f$ is assumed independent across sensors and snapshots, with each element following a complex Gaussian $\mathcal{CN}(0,\sigma^2)$.

The signals and noise are assumed to be statistically independent. The array covariance matrix is expressed as

$$\mathbb{E}[\mathbf{y}_{t_l,f}\mathbf{y}_{t_l,f}^{\mathsf{H}}]=\mathbf{A}\mathbb{E}[\mathbf{x}_{t_l,f}\mathbf{x}_{t_l,f}^{\mathsf{H}}]\mathbf{A}^{\mathsf{H}}+\mathbb{E}[\mathbf{e}_{t_l,f}\mathbf{e}_{t_l,f}^{\mathsf{H}}], \quad (3)$$

where $\mathbb{E}[\cdot]$ is the expectation across time t_l, at time t_l, $\mathbf{y}_{t_l,f}=[y_{1t_l,f}\dots y_{Mt_l,f}]^{\mathsf{T}}\in\mathbb{C}^M$, $\mathbf{x}_{t_l,f}=[x_{1t_l,f}\dots x_{Kt_l,f}]^{\mathsf{T}}\in\mathbb{C}^K$, $\mathbf{e}_{t_l,f}=[e_{1t_l,f}\dots e_{Mt_l,f}]^{\mathsf{T}}\in\mathbb{C}^M$, $l=1,\dots,L$, and $\mathbf{A}=[\mathbf{a}_f(\theta_1)\dots\mathbf{a}_f(\theta_K)]\in\mathbb{C}^{M\times K}$ with K true DOAs $\{\theta_1,\dots,\theta_K\}$.

The signal-to-noise ratio (SNR) is defined for one snapshot, $\mathrm{SNR}=20\log_{10}\left(\|\sum_{k=1}^K x_{kt_l,f}\mathbf{a}_f(\theta_k)\|_2/\|\mathbf{e}_{t_l,f}\|_2\right)$.

III. DF for DOA

This section reviews DF for DOA [21], [22].

A. Array data model using Hadamard product for DF

We model the array data for a single frequency as a sum of plane waves (1) and assume multi-frequencies arrive at the array at the same DOAs. To exploit the frequency difference, $\Delta f_i=f_i^{\mathrm{U}}-f_i^{\mathrm{L}}$, $f_i^{\mathrm{U}}>f_i^{\mathrm{L}}$, we utilize the Hadamard product ($\circ$) of upper-frequency data $\mathbf{Y}_{f_i^{\mathrm{U}}}$ and the complex conjugate of lower-frequency data $\mathbf{Y}_{f_i^{\mathrm{L}}}$ [21], giving $\mathbf{Z}_{\Delta f_i}\in\mathbb{C}^{M\times L}$,

$$\begin{aligned}\mathbf{Z}_{\Delta f_i}&=\mathbf{Y}_{f_i^{\mathrm{U}}}\circ\mathbf{Y}_{f_i^{\mathrm{L}}}^*=[\mathbf{y}_{t_1,f_i^{\mathrm{U}}}\dots\mathbf{y}_{t_L,f_i^{\mathrm{U}}}]\circ[\mathbf{y}_{t_1,f_i^{\mathrm{L}}}^*\dots\mathbf{y}_{t_L,f_i^{\mathrm{L}}}^*]\\&=\sum_{k=1}^K\mathbf{a}_{\Delta f_i}(\theta_k)\left[\mathbf{x}_{kL,f_i^{\mathrm{U}}}^{\mathsf{T}}\circ\mathbf{x}_{kL,f_i^{\mathrm{L}}}^{\mathsf{H}}\right]\\&+\sum_{\substack{k'=1\\k'\neq k''}}^K\sum_{k''=1}^K\left[\mathbf{a}_{f_i^{\mathrm{U}}}(\theta_{k'})\circ\mathbf{a}_{f_i^{\mathrm{L}}}^*(\theta_{k''})\right]\left[\mathbf{x}_{k'L,f_i^{\mathrm{U}}}^{\mathsf{T}}\circ\mathbf{x}_{k''L,f_i^{\mathrm{L}}}^{\mathsf{H}}\right]+\mathbf{E}_\Delta,\end{aligned} \quad (4)$$

$$\begin{aligned}\mathbf{a}_{\Delta f_i}(\theta)&=\mathbf{a}_{f_i^{\mathrm{U}}}(\theta)\circ\mathbf{a}_{f_i^{\mathrm{L}}}^*(\theta)\\&=\left[e^{-j2\pi\Delta f_i d_1\sin\theta/c}\dots e^{-j2\pi\Delta f_i d_M\sin\theta/c}\right]^{\mathsf{T}}.\end{aligned} \quad (5)$$

Compared to (1), the product $\mathbf{Z}_{\Delta f_i}$ (4) is a sum of steering vectors but in Δf_i, $\mathbf{a}_{\Delta f_i}(\theta)$ (5). Unlike the frequencies $\{f_i^{\mathrm{U}},f_i^{\mathrm{L}}\}$, the DF Δf_i can be below array aliasing frequency.

The cross-terms in (4) generate artifact DOAs $\{\theta_1^{\mathrm{a}},\dots,\theta_{K^2-K}^{\mathrm{a}}\}$ [Sec. III.D]. Let $\mathbf{X}_{\Delta f_i}^{\mathrm{t}}=[\mathbf{x}_{t_1,\Delta f_i}^{\mathrm{t}}\dots\mathbf{x}_{t_L,\Delta f_i}^{\mathrm{t}}]\in\mathbb{C}^{K\times L}$ be the true source components and $\mathbf{X}_{\Delta f_i}^{\mathrm{a}}=[\mathbf{x}_{t_1,\Delta f_i}^{\mathrm{a}}\dots\mathbf{x}_{t_L,\Delta f_i}^{\mathrm{a}}]\in\mathbb{C}^{(K^2-K)\times L}$ be the artifact source components. $\mathbf{X}_{\Delta f_i}^{\mathrm{t}}$ and $\mathbf{X}_{\Delta f_i}^{\mathrm{a}}$ are related to the source amplitudes $x_{kt_l,f_i^{\mathrm{U}}}$ and $x_{kt_l,f_i^{\mathrm{L}}}$, for the (k,l)-element,

$$\begin{aligned}x_{kt_l,\Delta f_i}^{\mathrm{t}}&=x_{k't_l,f_i^{\mathrm{U}}}x_{k''t_l,f_i^{\mathrm{L}}}^*,\quad\text{for } k'=k'',\\x_{kt_l,\Delta f_i}^{\mathrm{a}}&=x_{k't_l,f_i^{\mathrm{U}}}x_{k''t_l,f_i^{\mathrm{L}}}^*,\quad\text{for } k'\neq k'',\end{aligned} \quad (6)$$

where $k',k''=1,\dots,K$.

The product $\mathbf{Z}_{\Delta f_i}$ (4) is given by

$$\mathbf{Z}_{\Delta f_i}=\mathbf{A}_{\Delta f_i}^{\mathrm{t}}\mathbf{X}_{\Delta f_i}^{\mathrm{t}}+\mathbf{A}_{\Delta f_i}^{\mathrm{a}}\mathbf{X}_{\Delta f_i}^{\mathrm{a}}+\mathbf{E}_\Delta, \quad (7)$$

where $\mathbf{A}_{\Delta f_i}^{\mathrm{t}}=[\mathbf{a}_{\Delta f_i}(\theta_1)\dots\mathbf{a}_{\Delta f_i}(\theta_K)]\in\mathbb{C}^{M\times K}$ is the DF steering matrix (5) corresponding to the true DOAs and $\mathbf{A}_{\Delta f_i}^{\mathrm{a}}=[\mathbf{a}_{\Delta f_i}(\theta_1^{\mathrm{a}})\dots\mathbf{a}_{\Delta f_i}(\theta_{K^2-K}^{\mathrm{a}})]\in\mathbb{C}^{M\times(K^2-K)}$ is for the artifact DOAs.

The array covariance matrix of $\mathbf{z}_{t_l,\Delta f_i}$ has fourth-order components in $\mathbf{x}$ and is expressed as

$$\begin{aligned}\mathbb{E}[\mathbf{z}_{t_l,\Delta f_i}\mathbf{z}_{t_l,\Delta f_i}^{\mathsf{H}}]&=\mathbf{A}_{\Delta f_i}^{\mathrm{t}}\mathbb{E}[\mathbf{x}_{t_l,\Delta f_i}^{\mathrm{t}}\mathbf{x}_{t_l,\Delta f_i}^{\mathrm{tH}}]\mathbf{A}_{\Delta f_i}^{\mathrm{tH}}\\&+\mathbf{A}_{\Delta f_i}^{\mathrm{a}}\mathbb{E}[\mathbf{x}_{t_l,\Delta f_i}^{\mathrm{a}}\mathbf{x}_{t_l,\Delta f_i}^{\mathrm{aH}}]\mathbf{A}_{\Delta f_i}^{\mathrm{aH}}+\mathbb{E}[\mathbf{e}_{t_l,\Delta}\mathbf{e}_{t_l,\Delta}^{\mathsf{H}}],\end{aligned} \quad (8)$$

where, at time t_l, $\mathbf{z}_{t_l,\Delta f_i}=[z_{1t_l,\Delta f_i}\dots z_{Mt_l,\Delta f_i}]^{\mathsf{T}}\in\mathbb{C}^M$, $\mathbf{x}_{t_l,\Delta f_i}^{\mathrm{t}}=[x_{1t_l,\Delta f_i}^{\mathrm{t}}\dots x_{Kt_l,\Delta f_i}^{\mathrm{t}}]^{\mathsf{T}}\in\mathbb{C}^K$, $\mathbf{x}_{t_l,\Delta f_i}^{\mathrm{a}}=[x_{1t_l,\Delta f_i}^{\mathrm{a}}\dots x_{Kt_l,\Delta f_i}^{\mathrm{a}}]^{\mathsf{T}}\in\mathbb{C}^{K^2-K}$, and $\mathbf{e}_{t_l,\Delta}=[e_{1t_l,\Delta}\dots e_{Mt_l,\Delta}]^{\mathsf{T}}\in\mathbb{C}^M$.

The first term in (8) is similar to the first term in (3), but evaluated at Δf_i and shows the true DOAs in the quadri-covariance matrix. The second term with K^2-K components represents artifact DOAs. The challenge will be to reduce the effect of these in the following steps, although we are not directly using the covariance matrix.

B. CBF

CBF for one frequency f uses the data sample covariance matrix (SCM) $\mathbf{R}_f$ as an estimate of $\mathbb{E}[\mathbf{y}_{t_l,f}\mathbf{y}_{t_l,f}^{\mathsf{H}}]$ (3). For N potential DOAs $\bar{\boldsymbol{\theta}}=[\bar\theta_1\dots\bar\theta_N]^{\mathsf{T}}\in[-90^\circ,90^\circ)$, the beamformer power for CBF is then,

$$P_f^{\mathrm{CBF}}(\bar\theta_n)=\mathbf{a}_f^{\mathsf{H}}(\bar\theta_n)\mathbf{R}_f\mathbf{a}_f(\bar\theta_n),\quad n=1,\dots,N, \quad (9)$$

$$\mathbf{R}_f=\frac{1}{L}\sum_{l=1}^L\mathbf{y}_{t_l,f}\mathbf{y}_{t_l,f}^{\mathsf{H}}. \quad (10)$$

This gives aliasing for $f>c/(2d)$.

C. DF-CBF

DF DOA estimation uses the product $\mathbf{Z}_{\Delta f_i}$ (4) and the steering matrix built using $\mathbf{a}_{\Delta f_i}(\theta)$ (5). The CBF for DF DOA uses the DF-SCM $\mathbf{R}_{\Delta f_i}$ as an estimate of $\mathbb{E}[\mathbf{z}_{t_l,\Delta f_i}\mathbf{z}_{t_l,\Delta f_i}^{\mathsf{H}}]$ (8). For N potential DOAs $\bar{\boldsymbol{\theta}}=[\bar\theta_1\dots\bar\theta_N]^{\mathsf{T}}\in[-90^\circ,90^\circ)$, the DF-CBF power is then,

$$P_{\Delta f_i}^{\mathrm{DF-CBF}}(\bar\theta_n)=\mathbf{a}_{\Delta f_i}^{\mathsf{H}}(\bar\theta_n)\mathbf{R}_{\Delta f_i}\mathbf{a}_{\Delta f_i}(\bar\theta_n), \quad (11)$$

$$\begin{aligned}\mathbf{R}_{\Delta f_i}&=\frac{1}{L}\sum_{l=1}^L\mathbf{z}_{t_l,\Delta f_i}\mathbf{z}_{t_l,\Delta f_i}^{\mathsf{H}}\\&=\frac{1}{L}\sum_{l=1}^L\left(\mathbf{y}_{t_l,f_i^{\mathrm{U}}}\mathbf{y}_{t_l,f_i^{\mathrm{U}}}^{\mathsf{H}}\right)\circ\left(\mathbf{y}_{t_l,f_i^{\mathrm{L}}}\mathbf{y}_{t_l,f_i^{\mathrm{L}}}^{\mathsf{H}}\right)^*.\end{aligned} \quad (12)$$

Note that CBF for one frequency f uses $\mathbf{Y}_f$ (1), $\mathbf{a}_f(\theta)$ (2), and the data SCM, i.e., $\sum_{l=1}^L\mathbf{y}_{t_l,f}\mathbf{y}_{t_l,f}^{\mathsf{H}}/L$, thus averaging the single-snapshot SCM. The DF uses the Hadamard product of two array covariance matrices (12).

Figure 1 shows CBF and DF-CBF. CBF has aliasing, which increases with frequency. DF-CBF has a consistent K^2 number of DOAs across frequency. As the processing frequency is lowered, $\Delta f_i<f_i^{\mathrm{L}}$, the resolution of the beamformer deteriorates. The beamwidth of the main lobe increases, and this decreases the resolution. The cross-terms in (4) show artifact DOA patterns in the beamforming spectrum. K true DOAs have K^2-K artifact DOAs, determined

This work is licensed under a Creative Commons Attribution-NonCommercial-NoDerivatives 4.0 License. For more information, see https://creativecommons.org/licenses/by-nc-nd/4.0/

This article has been accepted for publication in IEEE Open Journal of Signal Processing. This is the author's version which has not been fully edited and content may change prior to final publication. Citation information: DOI 10.1109/OJSP.2024.3425284

by the frequency and true DOAs. DF processing can have aliasing when the frequency difference Δf_i exceeds the aliasing frequency ($\Delta f_i > f_{\text{alias}}$), see Fig. 2. K^2-K artifact DOAs are independent of aliasing.

D. Artifact DOA problem

The artifact DOA can be found by assuming the power $\mathbf{x}_{kL,f_i^{\mathrm{L}}} = \mathbf{x}_{kL,f_i^{\mathrm{U}}} = \mathbf{1}$, only retaining the cross terms in (4), and finding when the beam power is 1, [21]

$$\mathbf{a}_{\Delta f_i}(\tilde{\theta})^{\mathsf{T}} \Big[\sum_{\substack{k'=1 \\ k'\neq k''}}^{K} \sum_{k''=1}^{K} \mathbf{a}_{f_i^{\mathrm{U}}}(\theta_{k'}) \circ \mathbf{a}^*_{f_i^{\mathrm{L}}}(\theta_{k''}) \Big] = 1. \tag{13}$$

Solving this gives the artifact DOAs $\tilde{\theta}$

$$\tilde{\theta} = \sin^{-1}\Big(\frac{f_i^{\mathrm{U}} \sin\theta_{k'} - f_i^{\mathrm{L}} \sin\theta_{k''}}{f_i^{\mathrm{U}} - f_i^{\mathrm{L}}} + 2\xi \Big), \; k' \neq k'', \tag{14}$$

where ξ is an integer that represents the number of jumps that must be added or subtracted to return $\tilde{\theta} \in [-90°, 90°)$.

To give intuition, the artifact DOAs $\tilde{\theta}$ (14) vary based on lower frequencies f_i^{L} for constant Δf_i, see Fig. 3(top), and true DOAs θ_k, see Fig. 3(bottom).

Even with only one DF pair, we can obtain the true DOA. DF DOA provides K^2 DOA estimates. If we assume K out of K^2 are the true DOAs, the corresponding K^2-K artifact DOAs are given by (14). The K assumed true DOAs and K^2-K artifact DOAs are compared with the estimated K^2 DF DOA estimates, and by finding the matching case, we retrieve the true DOAs. Since DF DOA requires estimating K^2 DOAs, K^2 should be sufficiently less than the number of sensors.

We utilize sparse techniques to enable high-resolution estimation of K^2 DOAs in DF DOA. Sparse methods provide high-resolution DOA performance both with single and multiple snapshots.

IV. Sparse methods for DF DOA estimation

We explore sparse methods in support of DF for DOA, aiming for high resolution. For reference, we start with the gridded sparse approach with an angular search grid [Sec. IV.A] and focus on the gridless sparse technique using the atomic norm to address the grid mismatch issue [Sec. IV.B].

A gridded sparse method for DOA with DF [22] utilizes l_1 norm minimization for sparse processing and handles one-snapshot data $\mathbf{z}_{t_l,\Delta f_i} \in \mathbb{C}^M$. This work utilizes gridless ANM and handles multi-snapshot and multi-DF data [Sec. IV.B].

A. Gridded sparse processing

This section is only for reference as the paper is focused on gridless methods. For the noiseless measurement (1) with K true DOAs, the product of the noiseless data $\mathbf{Z}^\star_{\Delta f_i} \in \mathbb{C}^{M\times L}$ (4) has K^2 DOAs, including the true and artifact, see Fig. 4(a), i.e.,

$$\mathbf{Z}^\star_{\Delta f_i} = \sum_{k=1}^{K^2} \mathbf{a}_{\Delta f_i}(\theta_k) \mathbf{x}^{\star\mathsf{T}}_{kL,\Delta f_i}, \tag{15}$$

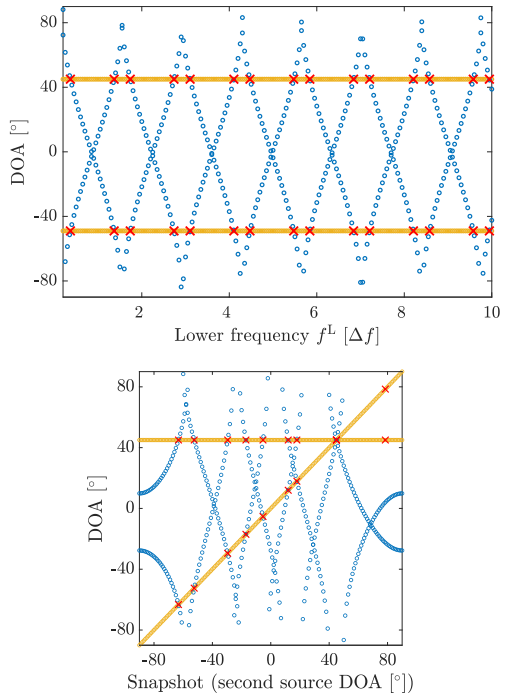

FIGURE 3. Predicted DF-DOA locations (14) (top) vs. lower frequency f^{L} with a constant DF $\Delta f_i = \Delta f$, and (bottom) moving DOA $[-90, 90]°$ at $f_1^{\mathrm{L}} = 4\Delta f$ with $\Delta f_1 = \Delta f$, thus $f_1^{\mathrm{U}} = 5\Delta f$. The plots show true DOAs (orange), the corresponding artifact DOAs (blue), and when true and artifact DOAs coincide (red ×). The ULA is as in Fig. 1.

where $\mathbf{x}^\star_{kL,\Delta f_i} = [x^\star_{kt_1,\Delta f_i} \dots x^\star_{kt_L,\Delta f_i}]^{\mathsf{T}} \in \mathbb{C}^L$, whose element is $x^\star_{kt_l,\Delta f_i}$, $k = 1,\dots,K^2$, $l = 1,\dots,L$. For N potential DOAs $\bar{\boldsymbol{\theta}} = [\bar{\theta}_1 \dots \bar{\theta}_N]^{\mathsf{T}} \in [-90°, 90°)$, the gridded DF DOA estimation, when there is no grid mismatch, is expressed as,

$$\mathbf{Z}_{\Delta f_i} = \mathbf{A}_{\Delta f_i} \mathbf{X}_{\Delta f_i} + \mathbf{E}_\Delta, \tag{16}$$

$$\mathbf{A}_{\Delta f_i} = [\mathbf{a}_{\Delta f_i}(\bar{\theta}_1) \dots \mathbf{a}_{\Delta f_i}(\bar{\theta}_N)], \tag{17}$$

where the complex source amplitude $\mathbf{X}_{\Delta f_i} \in \mathbb{C}^{N\times L}$ exhibits a K^2-row-sparse structure for $\mathbf{Z}^\star_{\Delta f_i}$ (15), see Fig. 4(b).

Sparse methods [31], [34], [47], [48] exploit the joint (row) sparsity of the solution to improve performance, which leads to the $l_{2,1}$ mixed-norm minimization problem,

$$\min_{\mathbf{X}_{\Delta f_i}} \frac{1}{2} \|\mathbf{Z}_{\Delta f_i} - \mathbf{A}_{\Delta f_i} \mathbf{X}_{\Delta f_i}\|_{\mathsf{F}}^2 + \tau^{(l_{2,1})} \|\mathbf{X}_{\Delta f_i}\|_{2,1}. \tag{18}$$

The regularization parameter $\tau^{(l_{2,1})} > 0$ balances the data fitting $\mathbf{A}_{\Delta f_i}\mathbf{X}_{\Delta f_i} - \mathbf{Z}_{\Delta f_i}$ and the (row) sparsity level in $\mathbf{X}_{\Delta f_i} \in \mathbb{C}^{N\times L}$. Joint sparsity on the rows $\mathbf{x}_{nL,\Delta f_i} \in \mathbb{C}^{1\times L}$, $n = 1,\dots,N$, is achieved by the $l_{2,1}$ mixed-norm, defined as

$$\|\mathbf{X}_{\Delta f_i}\|_{2,1} = \|\mathbf{x}^{(l_2)}_{\Delta f_i}\|_1, \tag{19}$$

$$\mathbf{x}^{(l_2)}_{\Delta f_i} = \big[\|\mathbf{x}_{1L,\Delta f_i}\|_2 \dots \|\mathbf{x}_{NL,\Delta f_i}\|_2 \big]^{\mathsf{T}}. \tag{20}$$

An inner l_2 norm is applied on the rows of $\mathbf{X}_{\Delta f_i}$, and an outer l_1 norm is applied on the vector of l_1 row-norms $\mathbf{x}^{(l_2)}_{\Delta f_i}$. The inner l_2 norm couples the elements in a row. Although it is appropriate to seek the solution with the minimum $l_{2,0}$ pseudo-norm, it leads to an NP-hard combinatorial problem,

This work is licensed under a Creative Commons Attribution-NonCommercial-NoDerivatives 4.0 License. For more information, see https://creativecommons.org/licenses/by-nc-nd/4.0/

This article has been accepted for publication in IEEE Open Journal of Signal Processing. This is the author's version which has not been fully edited and content may change prior to final publication. Citation information: DOI 10.1109/OJSP.2024.3425284.

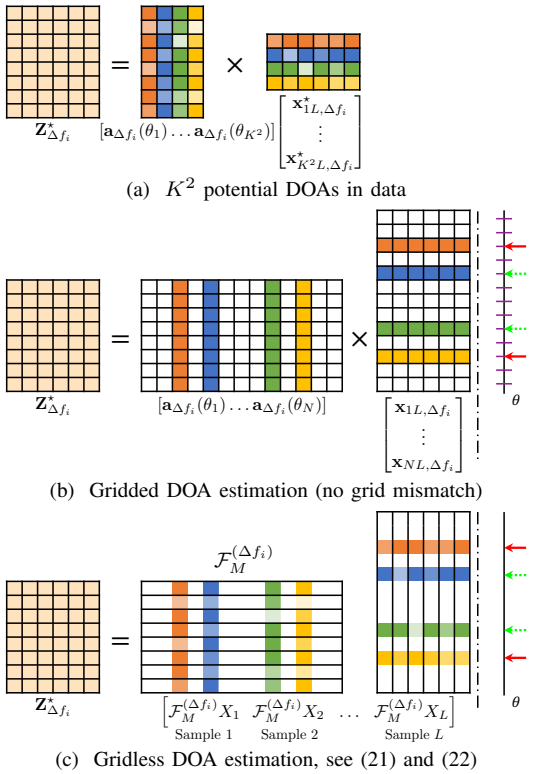

(a) K^2 potential DOAs in data

(b) Gridded DOA estimation (no grid mismatch)

(c) Gridless DOA estimation, see (21) and (22)

FIGURE 4. DF DOA estimation (16) **for noiseless data** (4) **($K=2$).**

which is computationally intractable. Convex relaxation with an $l_{2,1}$ mixed-norm is employed to obtain computationally tractable problems [31], [34], [47], [48].

B. Gridless sparse processing and atomic norm

Gridless sparse methods for DOA [31]–[33] are leveraged with DF. They operate directly in the continuous angle domain, thus, not needing to grid the look angles, cf. N potential DOAs (16). This enables resolving the grid mismatch problem [40], [41], [45], [46].

The sparse signal $\mathbf{x}^\star_{t_l,\Delta f_i}=[x^\star_{1t_l,\Delta f_i}\dots x^\star_{Kt_l,\Delta f_i}]^\mathsf{T}\in\mathbb{C}^K$ for the lth sample $\mathbf{z}^\star_{t_l,\Delta f_i}=[z^\star_{1t_l,\Delta f_i}\dots z^\star_{Mt_l,\Delta f_i}]^\mathsf{T}\in\mathbb{C}^M$ (15) having continuous θ is expressed as

$$X_l(\theta)=\sum_{k=1}^{K^2}x^\star_{kt_l,\Delta f_i}\delta(\theta-\theta_k), \tag{21}$$

where $x^\star_{kt_l,\Delta f_i}\in\mathbb{C}$ is the complex amplitude of the kth DOA for the lth sample $\mathbf{z}^\star_{t_l,\Delta f_i}$ and $\delta(\theta)$ is the Dirac delta function with $\theta\in[-90,90)$. The mth element of $\mathbf{Z}^\star_{\Delta f_i}$ for the lth sample is expressed as [45], [49], [50]

$$\begin{aligned}z^\star_{mt_l,\Delta f_i}&=\int_\theta e^{-j2\pi\Delta f_i d_m\sin\theta/c}X_l\mathrm{d}\theta\\&=\sum_{k=1}^{K^2}x^\star_{kt_l,\Delta f_i}e^{-j2\pi\Delta f_i d_m\sin\theta/c}=[\mathcal{F}_M^{(\Delta f_i)}X_l]_m,\end{aligned} \tag{22}$$

where the operator $\mathcal{F}_M^{(\Delta f_i)}$ maps the continuous signal X_l to the data $\mathbf{z}^\star_{t_l,\Delta f_i}\in\mathbb{C}^M$ so that $\mathbf{z}^\star_{t_l,\Delta f_i}=\mathcal{F}_M^{(\Delta f_i)}X_l$. For the gridded method (16), $\mathbf{A}_{\Delta f_i}$ (17) maps the gridded sparse signal $\mathbf{X}_{\Delta f_i}$ to the data $\mathbf{Z}^\star_{\Delta f_i}$, i.e., $\mathbf{Z}^\star_{\Delta f_i}=\mathbf{A}_{\Delta f_i}\mathbf{X}_{\Delta f_i}$. $\mathcal{F}_M^{(\Delta f_i)}$ is linear in amplitudes and nonlinear in DOAs: (for each $\alpha,\beta\in\mathbb{R}$)

$$\mathcal{F}_M^{(\Delta f_i)}[\alpha X_l(\theta)+\beta X_l(\theta)]=\alpha\mathcal{F}_M^{(\Delta f_i)}X_l(\theta)+\beta\mathcal{F}_M^{(\Delta f_i)}X_l(\theta), \tag{23}$$

$$\mathcal{F}_M^{(\Delta f_i)}X_l(\alpha\theta_1+\beta\theta_2)\neq\alpha\mathcal{F}_M^{(\Delta f_i)}X_l(\theta_1)+\beta\mathcal{F}_M^{(\Delta f_i)}X_l(\theta_2). \tag{24}$$

The data $\mathbf{Z}^\star_{\Delta f_i}$ (15) is expressed as $\mathbf{Z}^\star_{\Delta f_i}=[\mathcal{F}_M^{(\Delta f_i)}X_1\dots\mathcal{F}_M^{(\Delta f_i)}X_L]$, see Fig. 4(c).

In ANM [40], [41], [45], [46], $\mathbf{Z}^\star_{\Delta f_i}$(15) is considered as a convex combination of atoms $\mathbf{a}(\theta_k)\boldsymbol{\phi}_{kL}$ with $\boldsymbol{\phi}_{kL}^\mathsf{T}\in\mathbb{C}^L$, $\|\boldsymbol{\phi}_{kL}\|_2=1$ and the DOAs θ are continuous and thus gridless. The atomic norm of the noise-free $\mathbf{Z}^\star_{\Delta f_i}$ is defined as

$$\left\|\mathbf{Z}^\star_{\Delta f_i}\right\|_{\mathcal{A}}=\inf_{\substack{\xi_k,\\ \theta_k,\boldsymbol{\phi}_{kL}}}\left\{\sum_{k=1}^{K^2}\xi_k:\mathbf{Z}^\star_{\Delta f_i}=\sum_{k=1}^{K^2}\xi_k\mathbf{a}_{\Delta f_i}(\theta_k)\boldsymbol{\phi}_{kL}\right\}, \tag{25}$$

cf. the gridded method has $\mathbf{Z}^\star_{\Delta f_i}=\mathbf{A}_{\Delta f_i}\mathbf{X}_{\Delta f_i}$ (16). Regarding the support (nonzero rows) of $\mathbf{X}_{\Delta f_i}$ (16), $\mathbf{x}^\star_{kL,\Delta f_i}$, $k=1,\dots,K^2$, the kth component has the relation, $\mathbf{x}^\star_{kL,\Delta f_i}=\xi_k\boldsymbol{\phi}_{kL}$. Thus, the atomic norm (25) can be viewed as a continuous counterpart of the $l_{2,1}$ mixed-norm (19) used in the gridded setting, i.e., $\|\mathbf{Z}^\star_{\Delta f_i}\|_{\mathcal{A}}=\|\mathbf{X}^\star_{\Delta f_i}\|_{2,1}$.

The atomic norm (25) has the equivalent SDP [41],

$$\begin{aligned}\left\|\mathbf{Z}^\star_{\Delta f_i}\right\|_{\mathcal{A}}=\inf_{\mathbf{u}_{\Delta f_i},\mathbf{V}_L}\ &\frac{1}{2M}\mathrm{Tr}\big(\mathrm{Toep}(\mathbf{u}_{\Delta f_i})\big)+\frac{1}{2}\mathrm{Tr}(\mathbf{V}_L)\\ \text{s.t.}\ &\begin{bmatrix}\mathrm{Toep}(\mathbf{u}_{\Delta f_i})&\mathbf{Z}^\star_{\Delta f_i}\\ \mathbf{Z}^{\star\mathsf{H}}_{\Delta f_i}&\mathbf{V}_L\end{bmatrix}\succeq 0,\end{aligned} \tag{26}$$

where $\mathrm{Toep}(\mathbf{u}_{\Delta f_i})$ is a Toeplitz matrix related to the data covariance matrix, containing DOA information θ_k within the data $\mathbf{Z}^\star_{\Delta f_i}$ and $\mathbf{V}_L\in\mathbb{C}^{L\times L}$ is a free matrix variable.

Gridless sparse processing for noisy data $\mathbf{Z}_{\Delta f_i}$ (4) is formulated using the atomic norm (25) [51], [52],

$$\min_{\mathbf{Z}^\star_{\Delta f_i}}\ \frac{1}{2}\|\mathbf{Z}_{\Delta f_i}-\mathbf{Z}^\star_{\Delta f_i}\|_\mathsf{F}^2+\tau\|\mathbf{Z}^\star_{\Delta f_i}\|_{\mathcal{A}}, \tag{27}$$

where $\mathbf{Z}^\star_{\Delta f_i}$ is a measurement parameter to be estimated. The regularization parameter τ can be tuned as in (18). Using the equivalent SDP formulation (26), the SDP formulation of (27) is given by [41], [51], [52]

$$\begin{aligned}\min_{\substack{\mathbf{Z}^\star_{\Delta f_i},\\ \mathbf{u}_{\Delta f_i},\mathbf{V}_L}}\ &\frac{1}{2}\|\mathbf{Z}_{\Delta f_i}-\mathbf{Z}^\star_{\Delta f_i}\|_\mathsf{F}^2+\frac{\tau}{2}\Big(\frac{1}{M}\mathrm{Tr}\big(\mathrm{Toep}(\mathbf{u}_{\Delta f_i})\big)+\mathrm{Tr}(\mathbf{V}_L)\Big)\\ \text{s.t.}\ &\begin{bmatrix}\mathrm{Toep}(\mathbf{u}_{\Delta f_i})&\mathbf{Z}^\star_{\Delta f_i}\\ \mathbf{Z}^{\star\mathsf{H}}_{\Delta f_i}&\mathbf{V}_L\end{bmatrix}\succeq 0.\end{aligned} \tag{28}$$

The standard SDP solver CVX [53] is employed for (28).

C. DOA recovery

DOAs are encoded in $\mathrm{Toep}(\mathbf{u}_{\Delta f_i})$ (26). After solving (28) and obtaining $\mathrm{Toep}(\mathbf{u}_{\Delta f_i})$, we retrieve the DOAs using the

This work is licensed under a Creative Commons Attribution-NonCommercial-NoDerivatives 4.0 License. For more information, see https://creativecommons.org/licenses/by-nc-nd/4.0/

This article has been accepted for publication in IEEE Open Journal of Signal Processing. This is the author's version which has not been fully edited and content may change prior to final publication. Citation information: DOI 10.1109/OJSP.2024.3425284

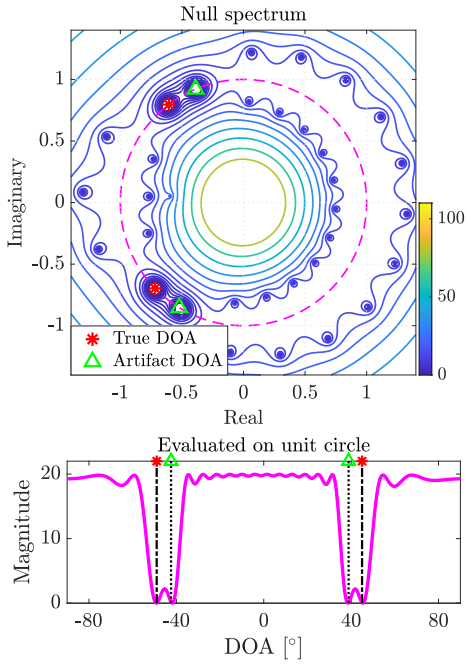

FIGURE 5. Null spectrum contour [dB] and evaluation on the unit circle with one DF data. The environment is as in Fig. 1 at $f^{\mathrm{L}}=10\Delta f$ and $f^{\mathrm{U}}=11\Delta f$.

Vandermonde decomposition of the Toeplitz matrix,

$$\mathrm{Toep}\big(\mathbf{u}_{\Delta f_i}\big)=\sum_{k=1}^{K^2}\xi\mathbf{a}_{\Delta f_i}(\theta_k)\mathbf{a}_{\Delta f_i}^{\mathsf{H}}(\theta_k)=\mathbf{A}_{\Delta f_i}^{\star}\mathrm{diag}(\boldsymbol{\xi})\mathbf{A}_{\Delta f_i}^{\star\mathsf{H}}, \tag{29}$$

$$\mathbf{A}_{\Delta f_i}^{\star}=[\mathbf{a}_{\Delta f_i}(\theta_1)\dots\mathbf{a}_{\Delta f_i}(\theta_{K^2})]. \tag{30}$$

Any positive semidefinite Toeplitz matrix $\mathrm{Toep}(\mathbf{u}_{\Delta f_i})\in\mathbb{C}^{M\times M}$ of rank $K^2\le M$ admits the atomic Vandermonde decomposition (29). The decomposition is unique if $K^2\le M$ [31, Theorem 11.5]. The Vandermonde decomposition (29) can be computed efficiently via root finding or by Prony's method [40], [48] or matrix pencil approaches [31], [54].

We employ the decomposition method [55, Sec. III.B] and the steps are:

1. Eigendecompose $\mathrm{Toep}(\mathbf{u}_{\Delta f_i})$ into signal- and noise-subspace, i.e.,
$$\mathrm{Toep}(\mathbf{u}_{\Delta f_i})=\mathbf{U}_S\boldsymbol{\Lambda}_S\mathbf{U}_S^{\mathsf{H}}+\mathbf{U}_N\boldsymbol{\Lambda}_N\mathbf{U}_N^{\mathsf{H}}. \tag{31}$$
2. Compute the null spectrum, given by
$$\mathcal{D}_{\Delta f_i}(z)=\mathbf{a}_{\Delta f_i}^{\mathsf{H}}(z)\mathbf{U}_N\mathbf{U}_N^{\mathsf{H}}\mathbf{a}_{\Delta f_i}(z), \tag{32}$$
$$z=e^{-j2\pi\Delta f_i d\sin\theta/c}, \tag{33}$$
$$\mathbf{a}_{\Delta f_i}(z)=[z^0\ z^1\dots z^{M-1}]^{\mathsf{T}}. \tag{34}$$
Recall the steering (2) and DF steering vectors (5).
3. Find the roots of $\mathcal{D}_{\Delta f_i}(z)$ in complex z-plane by localizing the K^2 lowest local minima of $\mathcal{D}_{\Delta f_i}(z)$ on the unit circle $|z|=1$ [55, Eq. (43)],
$$\hat{\boldsymbol{z}}=\underset{|z|=1}{\underset{k}{\mathrm{argmin}}}\ \mathcal{D}_{\Delta f_i}(z),\quad k=1,\dots,K^2. \tag{35}$$
Since $\mathbf{U}_N\perp\mathbf{a}_{\Delta f_i}(z_k)$ and $|z_k|=1$, the DOA θ_k encoded in z_k is associated with the K^2 roots of $\mathcal{D}_{\Delta f_i}(z)$ on the unit circle.

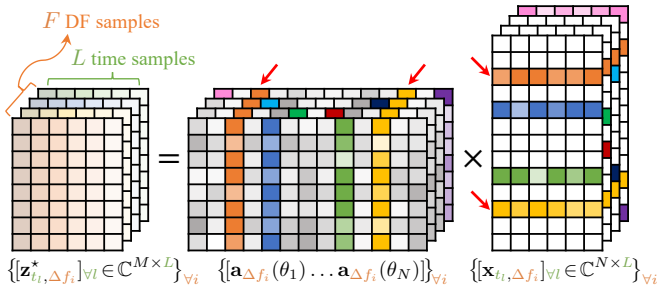

FIGURE 6. DF DOA estimation (16) for noiseless data (4) ($K=2$) with multiple observations: L time samples, $t_1,\dots,t_L$, and F DF samples, $f_1,\dots,f_F$. (a total LF samples) Note that, multiple time samples share a common $\mathbf{A}_{\Delta f_i}$, which multiple DF samples do not.

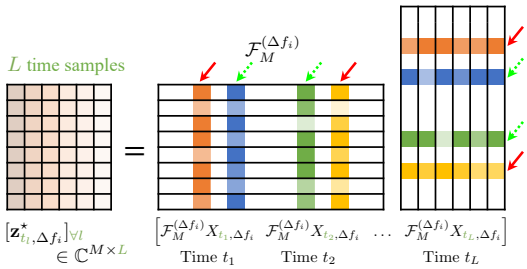

(a) Multi-snapshot model

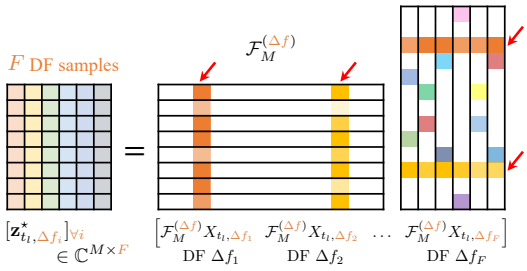

(b) Multi-DF model using a uniformly-spaced DF Δf

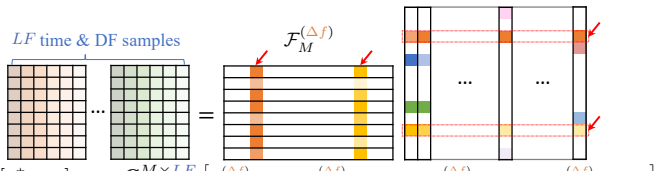

(c) (LF-)Multi-snapshot-DF model

FIGURE 7. Gridless sparse DF DOA estimation with MMVs: (a) multi-snapshot model (37) [the ANM (43)], (b) multi-DF model (39), and (c) multi-snapshot-DF model (40) [the ANM (42)].

4. DOAs are obtained by
$$\hat{\theta}_k=-\sin^{-1}\Big(\frac{c\angle\hat{z}_k}{2\pi\Delta f_i d}\Big). \tag{36}$$
5. Refine the amplitudes of the corresponding $\hat{\theta}_k$ using least squares and construct a K^2-rank Toeplitz matrix (29).

The null spectrum is plotted in Fig. 5. There are K true and K^2-K artifact DOAs, with changes in Δf_i, the true DOAs remain stationary while the artifact DOAs vary [Sec. VI.B].

This work is licensed under a Creative Commons Attribution-NonCommercial-NoDerivatives 4.0 License. For more information, see https://creativecommons.org/licenses/by-nc-nd/4.0/

This article has been accepted for publication in IEEE Open Journal of Signal Processing. This is the author's version which has not been fully edited and content may change prior to final publication. Citation information: DOI 10.1109/OJSP.2024.3425284.

V. Multiple time and frequency samples

Multiple measurement vector (MMV) processing deals with multiple observations simultaneously. Simultaneous sparse methods group MMVs into a matrix and recover sparse signals from MMVs. The condition for using MMV models is that they share the common support (sparsity profile) [Fig. 4]. Simultaneous MMV treatment outperforms single measurement vector (SMV) because it handles more data together. For stationary DOAs (DOAs are constant but amplitudes vary), sparse MMV models are ideal. In the following, we introduce a multi-snapshot MMV model with one DF and propose two methods to handle DF MMVs: multi-snapshot-DF [Sec. V.B] and multi-snapshot-DF-SA [Sec. V.C].

A. Single-DF multi-snapshot processing

Joint sparse DOA methods in Sec. IV are MMV models, which handle multiple L time snapshots as MMVs and a DF Δf_i as an SMV. As L MMVs $\mathbf{z}^{\star}_{t_l,\Delta f_i}$, $l=1,\ldots,L$, share the common K^2-sparsity profile, multi-snapshot processing is available, see Fig. 7(a). Multi-snapshot DOA estimation for a single DF Δf_i collects all snapshot data into one matrix, $\mathbf{Z}_{L,\Delta f_i}\in\mathbb{C}^{M\times L}$ (5),

$$\mathbf{Z}_{L,\Delta f_i} = [\mathbf{z}_{t_1,\Delta f_i}\ldots\mathbf{z}_{t_L,\Delta f_i}]\,. \tag{37}$$

L snapshot samples $\mathbf{z}^{\star}_{t_l,\Delta f_i}$, $l=1,\ldots,L$, share common dictionaries $\mathbf{a}_{\Delta f_i}(\theta_k)$ and a common K^2-sparsity profile.

F DF samples $\mathbf{z}^{\star}_{t_l,\Delta f_i}$, in contrast, have different dictionaries for each DF Δf_i, $i=1,\ldots,F$, i.e., $\mathbf{a}_{\Delta f_i}(\theta)\neq\mathbf{a}_{\Delta f_j}(\theta)$ $(i\neq j)$ and share a common K-sparsity profile for the true DOAs but not for the K^2-K artifact DOAs, see Fig. 7(b).

B. Multi-snapshot-DF with uniformly-spaced DFs

Consider the DF data $\mathbf{z}_{t_l,\Delta f_i}$, $i=1,\ldots,F$. If DFs are uniformly-spaced, $\Delta f_i=\Delta f$, $i=1,\ldots,F$, the DF-steering vector $\mathbf{a}_{\Delta f_i}(\theta)$ (5) is the same over F DF pairs, i.e.,

$$\mathbf{a}_{\Delta f}(\theta) = \mathbf{a}_{\Delta f_1}(\theta) = \ldots = \mathbf{a}_{\Delta f_F}(\theta). \tag{38}$$

This provides that $\mathbf{z}_{t_l,\Delta f_i}$, $i=1,\ldots,F$, share the same $\mathbf{a}_{\Delta f}(\theta)$ (38). Then we can concatenate F DF observations at time t_l and achieve multi-DF processing, see Fig. 7(b). Multi-DF DOA estimation for one snapshot t_l collects all DF data into one matrix, $\mathbf{Z}_{t_l,F}\in\mathbb{C}^{M\times F}$,

$$\mathbf{Z}_{t_l,F} = [\mathbf{z}_{t_l,\Delta f_1}\ldots\mathbf{z}_{t_l,\Delta f_F}]\,. \tag{39}$$

The L time samples are concatenated as each $\mathbf{z}_{t_l,\Delta f_i}$ shares the same DF-steering vectors $\mathbf{a}_{\Delta f_i}(\theta)$ (5) over L snapshots. Compared to the multi-snapshot [Fig. 7(a)], the multi-DF has artifact DOAs different across DFs Δf_i, $i=1,\ldots,F$ [Fig. 7(b)].

Uniformly-spaced DFs Δf enables multi-snapshot-DF processing, which treats all LF time and frequency observations jointly, see Fig. 7(c). The method is achieved by concatenating LF data, $\mathbf{Z}_{L,F}\in\mathbb{C}^{M\times LF}$, i.e.,

$$\mathbf{Z}_{L,F} = [\mathbf{z}_{t_1,\Delta f_1}\ldots\mathbf{z}_{t_L,\Delta f_1}\ldots\mathbf{z}_{t_1,\Delta f_F}\ldots\mathbf{z}_{t_L,\Delta f_F}]. \tag{40}$$

C. Multi-snapshot-DF-SA

We propose a method that handles L-time data jointly at each DF (the multi-snapshot [Sec. V.A]), solves the SDP (28) for F-DFs, and aggregates the sparse spectra across DFs using averaging from which the DOAs are extracted. While the artifact DOAs are inconsistent across DFs, the true DOAs remain consistent, see Fig. 7(b). Therefore, we can extract the true DOAs from consistent DOA estimates across DFs. An example of using MUSIC with spectral averaging (SA) to handle multiple DFs is in [3, Eq. (12)]. Unlike the multi-snapshot-DF [Sec. V.B], the multi-snapshot-DF-SA is not restricted to uniformly-spaced DFs.

As in Fig. 5, we calculate $\mathcal{D}_{\Delta f_i}(z_k)$ (34) in terms of θ instead of z, i.e., $\mathcal{D}_{\Delta f_i}(z_k)\rightarrow\mathcal{D}_{\Delta f_i}(\theta_k)$, $k=1,\ldots,K^2$, using the relation (36). The multi-snapshot-DF-SA obtains DOAs from averaging F spectra

$$\begin{aligned}\hat{\boldsymbol{\theta}} &= \underset{|z|=1}{\overset{k}{\operatorname{argmin}}}\ \frac{1}{F}\sum_{i=1}^{F}\mathcal{D}_{\Delta f_i}(\theta)\\ &= \underset{|z|=1}{\overset{k}{\operatorname{argmin}}}\ \frac{1}{F}\sum_{i=1}^{F}\mathbf{a}^{\mathsf{H}}_{\Delta f_i}(\theta)\mathbf{U}_i\mathbf{U}_i^{\mathsf{H}}\mathbf{a}_{\Delta f_i}(\theta),\end{aligned} \tag{41}$$

where $\mathbf{U}_i$ is the noise subspace $\mathbf{U}_N$ at DF Δf_i (31). Since the noise in each DF Δf_i is assumed statistically independent, averaging the spectra across DFs improves the DOA accuracy. The null spectra are in Fig. 9.

Averaging of the null spectrum (41) reduces the impact of noise, resulting in more reliable spectral minima at the true DOAs. Additionally, averaging provides robust estimates of the dominant DOAs across DFs for true DOAs and mitigates artifact DOAs.

D. SDP formulation

The implementation of the multi-snapshot-DF [Sec. V.B] and multi-snapshot-DF-SA [Sec. V.C] is done using $\mathbf{Z}_{L,F}\in\mathbb{C}^{M\times LF}$ (40) and $\mathbf{Z}_{L,\Delta f_i}\in\mathbb{C}^{M\times L}$ (37), $i=1,\ldots,F$, respectively.

We use the following steps for each method:

1) Multi-snapshot-DF [Sec. V.B] solves (28) with $\mathbf{Z}_{L,F}$ (40),

$$\begin{aligned}\min_{\substack{\mathbf{Z}^{\star}_{L,F},\\ \mathbf{u}_{\Delta f},\mathbf{V}_{LF}}}\ & \frac{1}{2}\|\mathbf{Z}_{L,F}-\mathbf{Z}^{\star}_{L,F}\|^2_{\mathsf{F}}\\ &+\frac{\tau}{2}\Big(\frac{1}{M}\mathrm{Tr}\big(\mathrm{Toep}(\mathbf{u}_{\Delta f})\big)+\mathrm{Tr}(\mathbf{V}_{LF})\Big)\\ \text{s.t.}\ & \begin{bmatrix}\mathrm{Toep}(\mathbf{u}_{\Delta f}) & \mathbf{Z}^{\star}_{L,F}\\ \mathbf{Z}^{\star\mathsf{H}}_{L,F} & \mathbf{V}_{LF}\end{bmatrix}\succeq 0.\end{aligned} \tag{42}$$

DOAs are extracted using $\mathrm{Toep}(\mathbf{u}_{\Delta f})$ (42) and Sec. IV.C.

2) Multi-snapshot-DF-SA [Sec. V.C] solves (28) with $\mathbf{Z}_{L,\Delta f_i}$ (37) for each Δf_i, $i=1,\ldots,F$,

$$\begin{aligned}\min_{\substack{\mathbf{Z}^{\star}_{L,\Delta f_i},\\ \mathbf{u}_{\Delta f_i},\mathbf{V}_L}}\ & \frac{1}{2}\|\mathbf{Z}_{L,\Delta f_i}-\mathbf{Z}^{\star}_{L,\Delta f_i}\|^2_{\mathsf{F}}\\ &+\frac{\tau}{2}\Big(\frac{1}{M}\mathrm{Tr}\big(\mathrm{Toep}(\mathbf{u}_{\Delta f_i})\big)+\mathrm{Tr}(\mathbf{V}_L)\Big)\\ \text{s.t.}\ & \begin{bmatrix}\mathrm{Toep}(\mathbf{u}_{\Delta f_i}) & \mathbf{Z}^{\star}_{L,\Delta f_i}\\ \mathbf{Z}^{\star\mathsf{H}}_{L,\Delta f_i} & \mathbf{V}_L\end{bmatrix}\succeq 0.\end{aligned} \tag{43}$$

DOAs are extracted using (41).

This work is licensed under a Creative Commons Attribution-NonCommercial-NoDerivatives 4.0 License. For more information, see https://creativecommons.org/licenses/by-nc-nd/4.0/

This article has been accepted for publication in IEEE Open Journal of Signal Processing. This is the author's version which has not been fully edited and content may change prior to final publication. Citation information: DOI 10.1109/OJSP.2024.3425284

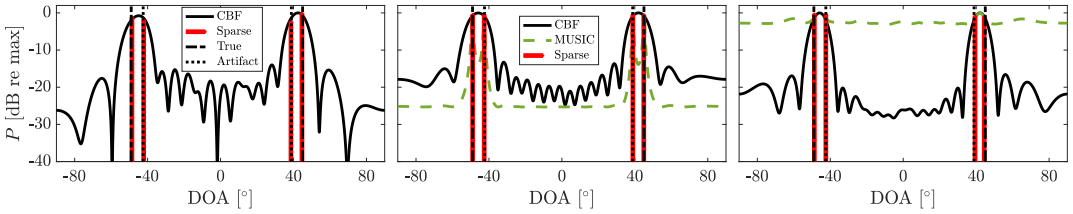

(a) Single time, single DF (b) Multiple time, single DF (c) Multiple time, coherent arrivals

FIGURE 8. **DOA spectra for $K=2$ equal-strength DOAs at $[-49, 45]^\circ$, $f^{\mathrm{L}}=10\Delta f$ ($F=1$), and SNR 20 dB using (a) one snapshot ($L=1$) and multiple snapshots ($L=25$) with (b) incoherent and (c) coherent arrivals.**

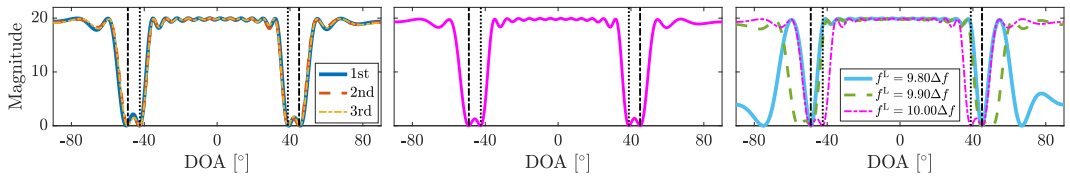

(a) Snapshot examples (single DF) (b) Multi-snapshot (single DF) (c) DF examples (multi-snapshot)

FIGURE 9. **Null spectrum $\mathcal{D}_{\Delta f_i}(\theta)$ (34) evaluated on unit circle for multi-snapshot processing [Sec. V.A]. The null spectrum $\mathcal{D}_{\Delta f_i}(\theta)$ for one snapshot: (a) 1st, 2nd, and 3rd snapshot, and for (b) multiple snapshots ($L=25$). The data in Fig. 8(b) is considered [multiple snapshots ($L=25$) and single DF ($F=1$)]. (c) The same environment as Fig. 9(b) but with DF pairs given by f^{L}: $9.80\Delta f$, $9.90\Delta f$, and $10.00\Delta f$.**

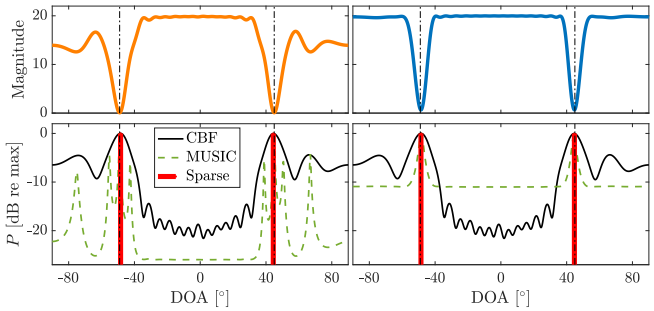

(a) Multi-snapshot-DF-SA (b) Multi-snapshot-DF

FIGURE 10. **(a) Multi-snapshot-DF-SA for DOA [Sec. V.C]. *Top:* Null spectrum and *Bottom:* the resulting DOA spectrum. Three $F=3$ null spectra in Fig. 9(c) are averaged. (b) Multi-snapshot-DF for DOA [Sec. V.B]. *Top:* Null spectrum and *Bottom:* the resulting DOA spectrum. A total of $LF=75$ samples [$L=25$ and $F=3$] are simultaneously processed.**

VI. Results

We present several results for our DF DOA estimation. First, we compare the beamforming spectra of the method to those of DF-CBF and DF-MUSIC [21] under various conditions. Next, we discuss results on multiple time and frequency samples and evaluate the DOA performance.

Various scenarios are considered, including single ($L=1$) and multiple ($L=25$) snapshots with one DF ($F=1$), coherent arrivals (multipath environment), in Figs. 8 and 9, and with multiple DFs ($F=3$) using the multi-snapshot-DF [Sec. V.B] and multi-snapshot-DF-SA [Sec. V.C] in Figs. 10 and 11.

We consider a ULA with $M=20$ elements with a spacing d. The frequencies are measured using the spatial aliasing frequency $\Delta f=(c/d)/2$. The DF is uniform for all pairs of frequencies, i.e., $\Delta f_i=\Delta f$, $i=1,\ldots,F$.

The DOA performance is evaluated based on the root-mean-squared error (RMSE), which is computed,

$$\mathrm{RMSE}=\sqrt{\mathbb{E}\left[\frac{1}{K}\sum_{k=1}^{K}\left(\hat{\theta}_k-\theta_k^{\mathrm{true}}\right)^2\right]}. \tag{44}$$

A. DF DOA estimation for each single DF

Figure 8(a) compares DF-CBF and sparse method in the case of one snapshot and one DF. DF-CBF fails to estimate all DOAs accurately due to its low resolution.

The multi-snapshot considers all snapshots simultaneously and seeks support across snapshots to improve estimation accuracy [Fig. 8(b)]. With multiple snapshot data, we can use DF-MUSIC [21], which provides high-resolution estimates for all DOAs. However, MUSIC cannot handle coherent arrivals [Fig. 8(c)]. In contrast, the gridless sparse method handles all scenarios.

B. Null spectra and the sparsity profiles in MMVs

Figure 9 shows the DOA recovery using null spectra $\mathcal{D}_{\Delta f_i}(\theta)$ (34), evaluated on the unit circle by locating the minimum points [Sec. IV.C]. The spectra for one snapshot show peaks at the true and artifact DOAs while sharing a common sparsity profile [Fig. 9(a)]. The multi-snapshot [Fig. 9(b)] exploits the shared support to achieve accurate estimates by handling all snapshots simultaneously.

The null spectra for the multi-snapshot-single-DF ($L=25$ and $F=1$) exhibit peaks at the true DOAs and artifact DOAs, see Fig. 9(c). Compared to Fig. 9(a), the polynomials across f^{L} share a common sparsity profile for the true DOAs but not for the artifacts [Fig. 9(c)].

Dealing with multiple DFs is illustrated: the multi-snapshot-DF [Sec. V.B] and multi-snapshot-DF-SA [Sec.

This work is licensed under a Creative Commons Attribution-NonCommercial-NoDerivatives 4.0 License. For more information, see https://creativecommons.org/licenses/by-nc-nd/4.0/

This article has been accepted for publication in IEEE Open Journal of Signal Processing. This is the author's version which has not been fully edited and content may change prior to final publication. Citation information: DOI 10.1109/OJSP.2024.3425284.

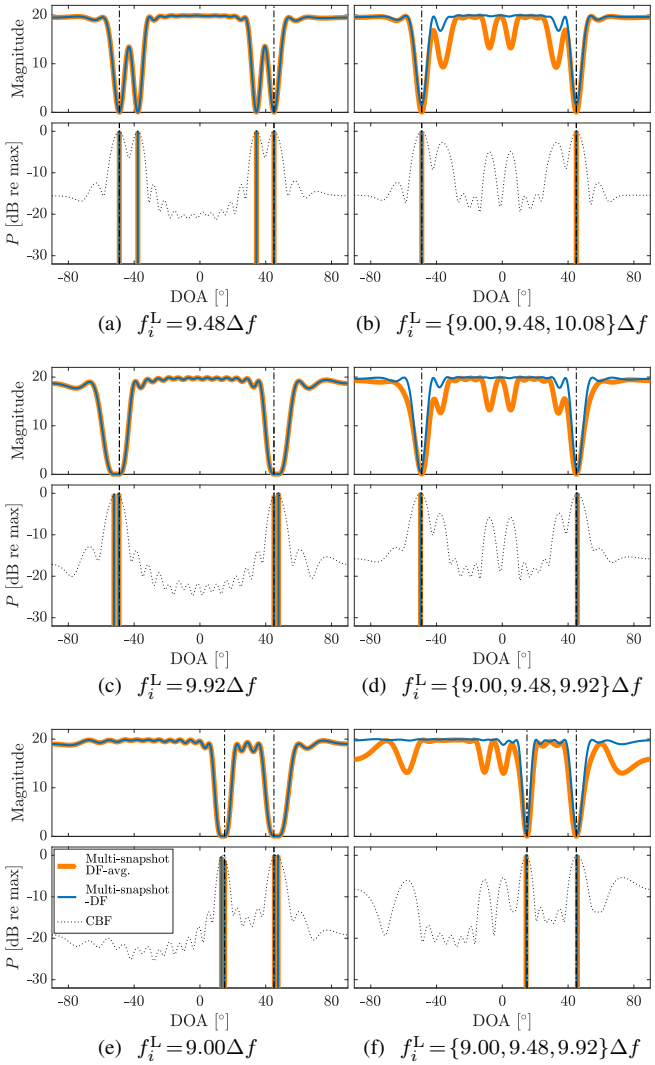

(a) $f_i^{\mathrm{L}} = 9.48\Delta f$ (b) $f_i^{\mathrm{L}} = \{9.00, 9.48, 10.08\}\Delta f$

(c) $f_i^{\mathrm{L}} = 9.92\Delta f$ (d) $f_i^{\mathrm{L}} = \{9.00, 9.48, 9.92\}\Delta f$

(e) $f_i^{\mathrm{L}} = 9.00\Delta f$ (f) $f_i^{\mathrm{L}} = \{9.00, 9.48, 9.92\}\Delta f$

FIGURE 11. Multi-snapshot-DF [Sec. V.B] and multi-snapshot-DF-SA [Sec. V.C] with different single DF (a,c) and multi-DF (b,d): CBF (dotted), multi-snapshot-DF-SA (orange), and multi-snapshot-DF (blue). In (a–d), DOAs are at $\{-49, 45\}^\circ$ at $\mathrm{SNR} = 20$ dB. RMSEs are (a) 0.03° (both), (b) 0.01° (orange) and 0.02° (blue), (c) 0.18° (both), and (d) 0.03° (orange) and 0.04° (blue). (e,f) As in (a,b,c,d), DOAs are at $\{15, 45\}^\circ$. RMSEs are (e) 0.16° (both) and (f) 0.01° (orange) and 0.02° (blue).

V.C]. The multi-snapshot-DF-SA solves (43) and recovers DOAs using (41) [Fig. 10(a)]. The multi-snapshot-DF solves (42) and recovers DOAs as in Sec. IV.C [Fig. 10(b)]. Both methods consider multiple DFs, enhancing the true DOAs while mitigating the artifacts.

C. Multiple DF data

We compare the performance of two methods for multiple DF data: the multi-snapshot-DF [Sec. V.B] and multi-snapshot-DF-SA [Sec. V.C]. We consider two scenarios as in Fig. 3. In the first example, all true and artifact DOAs are well-separated. In the second example, they are nearby.

Figure 11(a) has all true and artifact DOAs well-separated, leading to accurate DOA performance, RMSE 0.03°. In contrast, in Fig. 11(c), the minimum separation between true $\{-49, 45\}^\circ$ and artifact DOAs $\{-52.3, 48.1\}^\circ$ is only 3.1°. The sparse method can distinguish between them. However, the RMSE 0.18° increases relative to Fig. 11(a).

Multiple DF data give accurate DOA performance when all true DOAs and artifact DOAs are well-separated, see Fig. 11(b). Moreover, the multi-snapshot-DF-SA reduces DOA error when true and artifact DOAs are close, see Fig. 11(d). The averaging mitigates the error for $f_i^{\mathrm{L}} = 9.92\Delta f$, as the other $f_i^{\mathrm{L}} = 9.00\Delta f$ and $9.48\Delta f$ have the artifact at another location, resulting in improved performance, RMSE 0.03°.

Similar to the scenario where true and artifact DOAs coincide based on DF pairs in Fig. 3(left), a similar situation occurs based on DOA pairs, see Fig. 3(right). Figures 11(e) and 11(f) show a case having the true at $\{15, 45\}^\circ$ and artifact DOAs at $\{13.0, 47.9\}^\circ$, with a minimum separation of 2.0° between the true and artifact. The performance is similar to that of Figs. 11(c) and 11(d).

D. Bias of the multi-snapshot-DF

Dealing with multiple DFs offers improved DOA accuracy and mitigates errors when true and artifact DOAs are closely located. However, the multi-snapshot-DF performs worse than the multi-snapshot-DF-SA. For the multi-snapshot-DF, where multiple DF data are handled simultaneously [Sec. V.B and Figs. 7(b) and 7(c)], the artifact DOAs which vary across DFs impact the true DOAs, giving larger RMSE (0.04° [Fig. 11(d)] and 0.02° [Fig. 11(f)]) than the multi-snapshot-DF-SA (0.03° [Fig. 11(d)] and 0.01° [Fig. 11(f)]). This is because the nonlinear SDP used in the multi-snapshot-DF is less effective than the SA for closely spaced DOAs. Artifact DOAs show variations across DFs, reducing the multi-snapshot-DF performance.

E. SNR performance

We compare the RMSE (250 trials) of the DOA estimates produced by our approach to those obtained using existing methods including DF-CBF and DF-SBL [a DF version of sparse Bayesian learning (SBL) [56]–[62]] and the Cramér-Rao bound (CRB) [63, Eq. (110)] (considering DF data as MMVs). The gridded methods use a grid $[-90\!:\!0.005\!:\!90]^\circ$. We consider $L = 18$ snapshots. The lower frequencies of the DFs are $F = 25$ uniformly spaced in $f^{\mathrm{L}} \in [5\Delta f, 7.5\Delta f]$, and the paired upper frequencies are $f^{\mathrm{U}} = f^{\mathrm{L}} + \Delta f$.

Figure 12 presents three DOA scenarios: (a) one, (b) two, and (c) three DOAs. The sources have equal magnitude but each has random phases on $[0, 2\pi)$ at SNRs $[-15\!:\!3\!:\!30]$ dB.

For one DOA [Fig. 12(a)], all methods exhibit good results. The DF is beneficial in one DOA because it avoids artifact DOAs caused by cross-terms generated by multiple DOAs due to the product in the DF application.

For two DOAs [Fig. 12(b)], DF-CBF has bias from the interaction between the two main lobes near the corresponding DOAs (RMSE 0.1° at high SNR). In contrast, both multi-snapshot-DF-SA and multi-snapshot-DF perform better.

This work is licensed under a Creative Commons Attribution-NonCommercial-NoDerivatives 4.0 License. For more information, see https://creativecommons.org/licenses/by-nc-nd/4.0/

This article has been accepted for publication in IEEE Open Journal of Signal Processing. This is the author's version which has not been fully edited and content may change prior to final publication. Citation information: DOI 10.1109/OJSP.2024.3425284

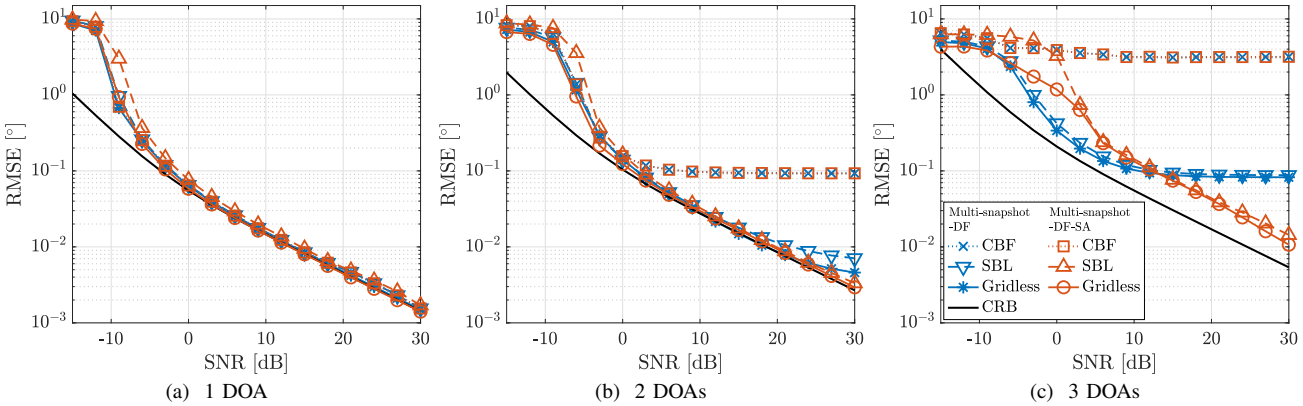

(a) 1 DOA (b) 2 DOAs (c) 3 DOAs

FIGURE 12. **RMSE vs. SNR of the simulated methods for (a) 1 DOA at $-45°$, (b) 2 DOAs at $[-45,-35]°$, and (c) 3 DOAs at $[-65,-3,2]°$.**

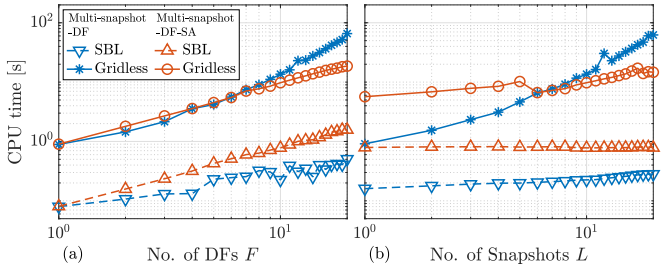

FIGURE 13. **(a) CPU times vs. number of snapshots L for $F=10$ and (b) CPU times vs. number of DFs F for $L=10$. 2 DOAs are at $[-49,45]°$.**

The multi-snapshot-DF-SA with gridless sparse processing shows a similar curve to that with SBL (also for the multi-snapshot-DF), as seen in Figs. 12(b) and 12(c). The estimates can be biased when DOAs are closely located in DF data, but well-spread-out DOAs give accurate estimates. With the DF-SA, since each DF is processed independently, averaging reduces the impact of the biased results.

The multi-snapshot-DF method, on the other hand, considers all DFs together. DFs with closely located DOAs and the other DFs with well-spread-out DOAs are processed simultaneously, leading to an overall bias in the results. It was shown [3], [21], [64], [65] that in multi-frequency DOA estimation, the multi-frequency (coherent) method performs worse than the averaging (incoherent) method in high SNRs due to this bias.

At high SNRs, the multi-snapshot-DF-SA, which estimates the DOA spectrum for each DF, outperforms the multi-snapshot-DF, see Fig. 12(c) for SNR >15 dB.

The advantage of the DF is its ability to process more DF data simultaneously. In low SNRs, where accurately estimating DOA for individual DFs is challenging, the DF outperforms the DF-SA despite the inherent bias, owing to the larger data being considered, see Fig. 12(c) for SNR -6 to 15 dB.

F. Complexity

The CPU times on an M2 MacBook Pro are shown in Fig. 13(a) vs. number of DFs F for $L=10$ and in Fig. 13(b) vs. number of snapshots L for $F=10$. The CPU time is mainly determined by solving the SDP. The multi-snapshot-DF-SA solves an SDP separately for each DF. The semidefinite constraint dimension is $(M+L)\times(M+L)$ (43), and this SDP is solved F times. The multi-snapshot-DF considers all LF data, solving an SDP once with a semidefinite constraint dimension of $(M+LF)\times(M+LF)$ (42). These SDP-based methods are slower than the SBL.

The DF-SA's CPU time increases linearly with F since it solves the SDP F times, see Fig. 13(a). The DF's CPU time increases more rapidly with increasing F due to the larger SDP constraint dimension LF. For $F\geq 6$, DF becomes slower than DF-SA. Figure 13(b) presents the CPU time as L varies with $F=10$. For $L<6$, the DF-SA, which repeats solving the SDP $F=10$ times, is slower than the DF. As L increases, the semidefinite constraint dimension in DF grows with LF. This gives slower CPU time for DF than DF-SA for $L\geq 6$.

VII. Conclusion

We derived an aliasing-free DOA estimator for high-frequency sources. It utilizes multiple frequency components of the source, particularly their frequency differences, to process signals at frequencies lower than the aliasing frequency, thus resolving spatial aliasing. However, this difference frequency (DF) application introduces unwanted (artifact) DOAs, necessitating a high-resolution DOA estimator for filtering.

To address this, we employed gridless sparse DOA processing. A gridless sparse method injects sparsity to obtain a sharp beamforming spectrum, enhancing resolution and estimating DOAs in the continuous angle domain to overcome grid mismatch. From the application perspective of this technique, we provided formulations for various scenarios when multiple data are measured in time and frequency: multi-snapshot-DF-SA and multi-snapshot-DF methods.

This work is licensed under a Creative Commons Attribution-NonCommercial-NoDerivatives 4.0 License. For more information, see https://creativecommons.org/licenses/by-nc-nd/4.0/

This article has been accepted for publication in IEEE Open Journal of Signal Processing. This is the author's version which has not been fully edited and content may change prior to final publication. Citation information: DOI 10.1109/OJSP.2024.3425284.

The performance indicates that the multi-snapshot-DF, which requires uniformly-spaced DFs and treats all time and frequency measurement data together, works best at low SNR, while the multi-snapshot-DF-SA, where each DF is handled individually and the null spectra are averaged across DFs for handling arbitrarily-spaced DFs, performs best at high SNR.

REFERENCES

[1] W. Liu and S. Weiss, *Wideband beamforming: concepts and techniques*, John Wiley & Sons, 2010.

[2] P. Gerstoft, W. S. Hodgkiss, W. A. Kuperman, H. C. Song, M. Siderius, and P. L. Nielsen, "Adaptive beamforming of a towed array during a turn," *IEEE J. Ocean. Eng.*, vol. 28, no. 1, pp. 44–54, Jan. 2003.

[3] Y.-S. Yoon, L. M. Kaplan, and J. H. McClellan, "TOPS: New DOA estimator for wideband signals," *IEEE Trans. Signal Process.*, vol. 54, no. 6, pp. 1977–1989, Jun. 2006.

[4] A. K. Shaw, "Improved wideband DOA estimation using modified TOPS (mTOPS) algorithm," *IEEE Signal Process. Lett.*, vol. 23, no. 12, pp. 1697–1701, Dec. 2016.

[5] E. D. Di Claudio, R. Parisi, and G. Jacovitti, "Space time MUSIC: Consistent signal subspace estimation for wideband sensor arrays," *IEEE Trans. Signal Process.*, vol. 66, no. 10, pp. 2685–2699, May 2018.

[6] E. BouDaher, Y. Jia, F. Ahmad, and M. G. Amin, "Multi-frequency co-prime arrays for high-resolution direction-of-arrival estimation," *IEEE Trans. Signal Process.*, vol. 63, no. 14, pp. 3797–3808, May 2015.

[7] Q. Shen, W. Liu, W. Cui, S. Wu, Y. D. Zhang, and M. G. Amin, "Focused compressive sensing for underdetermined wideband DOA estimation exploiting high-order difference coarrays," *IEEE Signal Process. Lett.*, vol. 24, no. 1, pp. 86–90, Dec. 2016.

[8] S. Qin, Y. D. Zhang, M. G. Amin, and B. Himed, "DOA estimation exploiting a uniform linear array with multiple co-prime frequencies," *Signal Process.*, vol. 130, pp. 37–46, Jan. 2017.

[9] F. Wang, Z. Tian, G. Leus, and J. Fang, "Direction of arrival estimation of wideband sources using sparse linear arrays," *IEEE Trans. Signal Process.*, vol. 69, pp. 4444–4457, Jul. 2021.

[10] S. Zhang, A. Ahmed, Y. D. Zhang, and S. Sun, "Enhanced DOA estimation exploiting multi-frequency sparse array," *IEEE Trans. Signal Process.*, vol. 69, pp. 5935–5946, Oct. 2021.

[11] C. L. Nikias and J. M. Mendel, "Signal processing with higher-order spectra," *IEEE Signal Process. Mag.*, vol. 10, no. 3, pp. 10–37, Jul. 1993.

[12] Q. Shen, W. Liu, W. Cui, and S. Wu, "Extension of co-prime arrays based on the fourth-order difference co-array concept," *IEEE Signal Process. Lett.*, vol. 23, no. 5, pp. 615–619, Mar. 2016.

[13] A. Ahmed, Y. D. Zhang, and B. Himed, "Effective nested array design for fourth-order cumulant-based DOA estimation," in *Proc. IEEE RadarConf*, 2017, pp. 998–1002.

[14] Q. Shen, W. Liu, W. Cui, S. Wu, and P. Pal, "Simplified and enhanced multiple level nested arrays exploiting high-order difference co-arrays," *IEEE Trans. Signal Process.*, vol. 67, no. 13, pp. 3502–3515, May 2019.

[15] S. Ren, W. Dong, X. Li, W. Wang, and X. Li, "Extended nested arrays for consecutive virtual aperture enhancement," *IEEE Signal Process. Lett.*, vol. 27, pp. 575–579, Mar. 2020.

[16] A. B. Gershman and H. Messer, "Robust mixed-order root-MUSIC," *Circuits Syst. Signal Process.*, vol. 19, no. 5, pp. 451–466, Oct. 2000.

[17] Z. Yang, Q. Shen, W. Liu, Y. C. Eldar, and W. Cui, "High-order cumulants based sparse array design via fractal geometries—part I: structures and DOFs," *IEEE Trans. Signal Process.*, vol. 71, pp. 327–342, Feb. 2023.

[18] S. Lu, F. Liu, Y. Li, K. Zhang, H. Huang, J. Zou, X. Li, Y. Dong, F. Dong, J. Zhu, Y. Xiong, W. Yuan, Y. Cui, and L. Hanzo, "Integrated sensing and communications: Recent advances and ten open challenges," *IEEE Internet Things J.*, vol. 11, no. 11, pp. 19094–20120, Feb. 2024.

[19] K. Sarabandi, "Δk-radar equivalent of interferometric SAR's: a theoretical study for determination of vegetation height," *IEEE Trans. Geosci. Remote Sens.*, vol. 35, no. 5, pp. 1267–1276, Sep. 1997.

[20] S. H. Abadi, H. C. Song, and D. R. Dowling, "Broadband sparse-array blind deconvolution using frequency-difference beamforming," *J. Acoust. Soc. Am.*, vol. 132, no. 5, pp. 3018–3029, Nov. 2012.

[21] Y. Park, P. Gerstoft, and J.-H. Lee, "Difference-frequency MUSIC for DOAs," *IEEE Signal Process. Lett.*, vol. 29, pp. 2612–2616, Dec. 2022.

[22] J.-H. Lee, Y. Park, and P. Gerstoft, "Compressive frequency-difference direction-of-arrival estimation," *J. Acoust. Soc. Am.*, vol. 154, no. 1, pp. 141–151, Jul. 2023.

[23] A. S. Douglass, H. C. Song, and D. R. Dowling, "Performance comparisons of frequency-difference and conventional beamforming," *J. Acoust. Soc. Am.*, vol. 142, no. 3, pp. 1663–1673, Sep. 2017.

[24] L. Xie, C. Sun, and J. Tian, "Deconvolved frequency-difference beamforming for a linear array," *J. Acoust. Soc. Am.*, vol. 148, no. 6, pp. EL440–EL446, Dec. 2020.

[25] L. Yang, Y. Wang, and Y. Yang, "Aliasing-free broadband direction of arrival estimation using a frequency-difference technique," *J. Acoust. Soc. Am.*, vol. 150, no. 6, pp. 4256–4267, Dec. 2021.

[26] X. Wang, H. Sun, L. Zhang, C.Dong, and L. Guo, "Unambiguous broadband direction of arrival estimation based on improved extended frequency-difference method," *J. Acoust. Soc. Am.*, vol. 152, no. 6, pp. 3281–3293, Dec. 2022.

[27] D. Kim, G. Byun, and J. Kim, "Direction-of-arrival estimation based on frequency difference–wavenumber analysis for sparse vertical array configuration," *Sensors*, vol. 23, no. 1, pp. 337, Dec. 2023.

[28] B. M. Worthmann, H. C. Song, and D. R. Dowling, "High frequency source localization in a shallow ocean sound channel using frequency difference matched field processing," *J. Acoust. Soc. Am.*, vol. 138, no. 6, pp. 3549–3562, Dec. 2015.

[29] D. J. Geroski and D. R. Dowling, "Long-range frequency-difference source localization in the Philippine sea," *J. Acoust. Soc. Am.*, vol. 146, no. 6, pp. 4727–4739, Dec. 2021.

[30] Z. Yuan, H. Niu, Z. Li, and W. Luo, "Difference frequency coherent matched autoproduct processing for source localization in deep ocean," *J. Acoust. Soc. Am.*, vol. 153, no. 4, pp. 2131–2147, Apr. 2023.

[31] Z. Yang, J. Li, P. Stoica, and L. Xie, "Sparse methods for direction-of-arrival estimation," in *Academic Press Library in Signal Processing: Array, Radar and Communications Engineering*, vol. 7, chapter 11, pp. 509–581. Academic Press, 2018.

[32] A. Xenaki and P. Gerstoft, "Grid-free compressive beamforming," *J. Acoust. Soc. Am.*, vol. 137, no. 4, pp. 1923–1935, Apr. 2015.

[33] Y. Park, Y. Choo, and W. Seong, "Multiple snapshot grid free compressive beamforming," *J. Acoust. Soc. Am.*, vol. 143, no. 6, pp. 3849–3859, Jun. 2018.

[34] D. Malioutov, M. Cetin, and A. S. Willsky, "A sparse signal reconstruction perspective for source localization with sensor arrays," *IEEE Trans. Signal Process.*, vol. 53, no. 8, pp. 3010–3022, Aug. 2005.

[35] Z.-M. Liu, Z.-T. Huang, and Y.-Y. Zhou, "Direction-of-arrival estimation of wideband signals via covariance matrix sparse representation," *IEEE Trans. Signal Process.*, vol. 59, no. 9, pp. 4256–4270, Sep. 2011.

[36] Z. Tang, G. Blacquiere, and G. Leus, "Aliasing-free wideband beamforming using sparse signal representation," *IEEE Trans. Signal Process.*, vol. 59, no. 7, pp. 3464–3469, Jul. 2011.

[37] Z.-Q. He, Z.-P. Shi, L. Huang, and H. C. So, "Underdetermined DOA estimation for wideband signals using robust sparse covariance fitting," *IEEE Signal Process. Lett.*, vol. 22, no. 4, pp. 435–439, Apr. 2014.

[38] S. Nannuru, K. L. Gemba, P. Gerstoft, W. S. Hodgkiss, and C. F. Mecklenbräuker, "Sparse Bayesian learning with multiple dictionaries," *Signal Process.*, vol. 159, pp. 159–170, Feb. 2019.

[39] Y. Wu, M. B. Wakin, and P. Gerstoft, "Gridless DOA estimation under the multi-frequency model," in *Proc. IEEE ICASSP*, 2022, pp. 5982–5986.

[40] Y. Chi and M. Ferreira Da Costa, "Harnessing sparsity over the continuum: Atomic norm minimization for superresolution," *IEEE Signal Process. Mag.*, vol. 37, no. 2, pp. 39–57, Mar. 2020.

[41] G. Tang, B. N. Bhaskar, P. Shah, and B. Recht, "Compressed sensing off the grid," *IEEE Trans. Inf. Theory*, vol. 59, no. 11, pp. 7465–7490, Nov. 2013.

[42] Y. Chi, L. L. Scharf, A. Pezeshki, and A. R. Calderbank, "Sensitivity to basis mismatch in compressed sensing," *IEEE Trans. Signal Process.*, vol. 59, no. 5, pp. 2182–2195, May 2011.

This work is licensed under a Creative Commons Attribution-NonCommercial-NoDerivatives 4.0 License. For more information, see https://creativecommons.org/licenses/by-nc-nd/4.0/

This article has been accepted for publication in IEEE Open Journal of Signal Processing. This is the author's version which has not been fully edited and content may change prior to final publication. Citation information: DOI 10.1109/OJSP.2024.3425284

[43] P. Pal and P. P. Vaidyanathan, "A grid-less approach to underdetermined direction of arrival estimation via low rank matrix denoising," *IEEE Signal Process. Lett.*, vol. 21, no. 6, pp. 737–741, Jun. 2014.
[44] Z. Yang, L. Xie, and C. Zhang, "Space time MUSIC: Consistent signal subspace estimation for wideband sensor arrays," *IEEE Trans. Signal Process.*, vol. 61, no. 1, pp. 38–43, Jan. 2013.
[45] E.J. Candès and C. Fernandez-Granda, "Towards a mathematical theory of super-resolution," *Commun. Pure Appl. Math.*, vol. 67, no. 6, pp. 906–956, Apr. 2014.
[46] Z. Yang and L. Xie, "On gridless sparse methods for line spectral estimation from complete and incomplete data," *IEEE Trans. Signal Process.*, vol. 63, no. 12, pp. 3139–3153, Jun. 2015.
[47] P. Gerstoft, A. Xenaki, and C. F. Mecklenbräuker, "Multiple and single snapshot compressive beamforming," *J. Acoust. Soc. Am.*, vol. 138, no. 4, pp. 2003–2014, Oct. 2015.
[48] C. Steffens, M. Pesavento, and M. E. Pfetsch, "A compact formulation for the $\ell_{2,1}$ mixed-norm minimization problem," *IEEE Trans. Signal Process.*, vol. 66, no. 6, pp. 1483–1497, Mar. 2018.
[49] E.J. Candès and C. Fernandez-Granda, "Super-resolution from noisy data," *J. Fourier Anal. Appl.*, vol. 19, pp. 1229–1254, Aug. 2013.
[50] C. Fernandez-Granda, "Super-resolution of point sources via convex programming," *Inf. Inference*, vol. 5, no. 3, pp. 251–303, Apr. 2016.
[51] B. N. Bhaskar, G. Tang, and B. Recht, "Atomic norm denoising with applications to line spectral estimation," *IEEE Trans. Signal Process.*, vol. 61, no. 23, pp. 5987–5999, Dec. 2013.
[52] Y. Chi and Y. Li, "Off-the-grid line spectrum denoising and estimation with multiple measurement vectors," *IEEE Trans. Signal Process.*, vol. 64, no. 5, pp. 1257–1269, Oct. 2016.
[53] M. Grant and S. Boyd, "CVX: Matlab software for disciplined convex programming, version 2.2," 2014, (Last viewed June 20, 2023).
[54] H. Groll, P. Gerstoft, M. Hofer, J. Blumenstein, T. Zemen, and C. F. Mecklenbräuker, "Scatterer identification by atomic norm minimization in vehicular mm-Wave propagation channels," *IEEE Access*, vol. 10, pp. 102334–102354, Sep. 2022.
[55] M. Wagner, Y. Park, and P. Gerstoft, "Gridless DOA estimation and root-MUSIC for non-uniform linear arrays," *IEEE Trans. Signal Process.*, vol. 69, pp. 2144–2157, Mar. 2021.
[56] M. E. Tipping, "Sparse Bayesian learning and the relevance vector machine," *J. Mach. Learn. Res.*, vol. 1, pp. 211–244, Jun. 2001.
[57] D. P. Wipf and B. D. Rao, "Sparse Bayesian learning for basis selection," *IEEE Trans. Signal Process.*, vol. 52, no. 8, pp. 2153–2164, Jul. 2004.
[58] Z. Yang, L. Xie, and C. Zhang, "Off-grid direction of arrival estimation using sparse Bayesian inference," *IEEE Trans. Signal Process.*, vol. 61, no. 1, pp. 38–43, Oct. 2012.
[59] P. Gerstoft, C. F. Mecklenbräuker, A. Xenaki, and S. Nannuru, "Multisnapshot sparse Bayesian learning for DOA," *IEEE Signal Process. Lett.*, vol. 23, no. 10, pp. 1469–1473, Oct. 2016.
[60] P. Chen, Z. Cao, Z. Chen, and X. Wang, "Off-grid DOA estimation using sparse Bayesian learning in MIMO radar with unknown mutual coupling," *IEEE Trans. Signal Process.*, vol. 67, no. 1, pp. 208–220, Nov. 2018.
[61] J. Dai and H. C. So, "Sparse Bayesian learning approach for outlier-resistant direction-of-arrival estimation," *IEEE Trans. Signal Process.*, vol. 66, no. 3, pp. 744–756, Nov. 2018.
[62] R. R. Pote and B. D. Rao, "Maximum likelihood-based gridless DOA estimation using structured covariance matrix recovery and SBL with grid refinement," *IEEE Trans. Signal Process.*, vol. 71, pp. 802–815, Mar. 2023.
[63] H. L. Van Trees, *Optimum Array Processing (Detection, Estimation, and Modulation Theory, Part IV)*, John Wiley & Sons, New York, 2002.
[64] H. Wang and M. Kaveh, "Coherent signal-subspace processing for the detection and estimation of angles of arrival of multiple wide-band sources," *IEEE Trans. Acoust., Speech, Signal Process.*, vol. 33, no. 4, pp. 823–831, Aug. 1985.
[65] D. N. Swingler and J. Krolik, "Source location bias in the coherently focused high-resolution broad-band beamformer," *IEEE Trans. Acoust., Speech, Signal Process.*, vol. 37, no. 1, pp. 143–145, Jan. 1989.

This work is licensed under a Creative Commons Attribution-NonCommercial-NoDerivatives 4.0 License. For more information, see https://creativecommons.org/licenses/by-nc-nd/4.0/